ROYAL SOCIETY
OF CHEMISTRY

PAPER

Check for updates

The hidden cost of solvent exchange: how mechanical damage compromises Ti₃C₂Tₓ MXene nanosheet properties

Ken Aldren S. Usman, [ID] *[a] Rochelle P. Ibabao, [ID] [a] Kim Marie D. Sisican, [ID] [a] Mia Judicpa, [ID] [a] Rufus Mart Ceasar R. Ramos, [ID] [a] Kevinilo P. Marquez,[ab] Jizhen Zhang, [ID] [ac] Elmer S. Austria, Jr, [ID] [d] Behnam Akhavan, [ID] [def] Anupma Thakur, [ID] [g] Nithin Chandran B. S., [ID] [g] Luke C. Henderson, [ID] [a] Babak Anasori [ID] [gh] and Joselito M. Razal [ID] *[ai]

Ti₃C₂Tₓ MXene nanosheets (hereafter "MXene") demonstrate great potential for applications in wearable electronics, sensors, energy storage, biomedical devices, and electromagnetic interference shielding. Their richly functionalized surfaces enable redispersion from water into polar organic solvents, offering flexibility for processing using non-aqueous inks. However, this solvent exchange process, typically achieved through vigorous vortex mixing, reduces the electrical conductivity of the resulting material. While this decrease has been attributed to increased interlayer spacing due to solvent intercalation, we show that mechanical agitation during solvent exchange directly causes sheet damage. Our results indicate that different redispersion conditions produce MXene sheets with varying degrees of damage and oxidation, which in turn lead to decreased conductivity. This drop persists even with volatile solvents and after annealing up to 200 °C. Furthermore, reversing the process by exchanging the organic solvent back to water, thereby restoring the interlayer spacing, still yields lower conductivity than pristine MXene. Collectively, these results indicate that mechanical sheet degradation is irreversible. We anticipate that recognizing the critical role of processing-induced damage will guide researchers in developing optimized MXene processing conditions to achieve desired material properties for specific applications.

Introduction

Since their discovery in 2011,[1] two-dimensional (2D) early transition metal carbides and/or nitrides, known as "MXenes" (with the general formula $M_{n+1}X_nT_x$, where $n = 1$ to 4, M is an early transition metal, X is carbon and/or nitrogen, and T_x represents surface terminations such as –F, –O, –Cl and/or –

[a]Institute for Frontier Materials, Deakin University, Geelong, VIC 3216, Australia. E-mail: k.usman@deakin.edu.au

[b]Institute of Chemistry, University of the Philippines Los Baños, Laguna 4031, Philippines

[c]Research Center for Materials Nanoarchitectonics, National Institute for Materials Science, Tsukuba 305-0044, Japan

[d]School of Biomedical Engineering, Faculty of Engineering, University of Sydney, Sydney, NSW 2006, Australia

[e]School of Engineering, University of Newcastle, Callaghan, NSW 2308, Australia

[f]Hunter Medical Research Institute, Precision Medicine Program, New Lambton Heights NSW, 2305, Australia

[g]School of Materials Engineering, Purdue University, West Lafayette, IN, 47907, USA

[h]School of Mechanical Engineering, Purdue University, West Lafayette, IN, 47907, USA

[i]Joint Research Centre for Fiber Innovations and Renewable Materials, School of Fashion and Textiles, The Hong Kong Polytechnic University, Hong Kong SAR, 999077, China. E-mail: joselito.razal@polyu.edu.hk

OH), have garnered significant attention due to their unique properties including exceptional electrical conductivity and electrochemical reactivity.[1–3] For instance, titanium carbide (Ti₃C₂Tₓ) MXene exhibits outstanding electrical conductivity (∼20 000 to 24 000 S cm⁻¹)[4,5] and electrochemical capacitance (>2800 F cm⁻³),[6] values that remain unmatched by other 2D nanomaterial, such as reduced graphene oxide.[7,8] These properties make MXenes highly suitable for energy storage devices, including supercapacitors and batteries, where they deliver high capacity and rapid charge–discharge rates.[9] Additionally, their lamellar structure and excellent electrical conductivity enable effective electromagnetic interference (EMI) shielding.[10] They also find applications in water purification[11] and gas sensing[12] due to their tunable surface chemistry and high surface area. Furthermore, their biocompatibility supports uses in biomedical fields such as drug delivery[13] and biosensing.[14]

Compared to other 2D materials, MXenes exhibit exceptional dispersibility in water (zeta potential of −30 to −60 mV) and numerous polar organic solvents,[15] enabling solution processing without stabilizers or surfactants.[16,17] This broad solvent compatibility has advanced the study of their rheological properties,[7,18] and facilitated their use in traditional processing methods to fabricate multifunctional, free-standing macro-

This journal is © The Royal Society of Chemistry 2026

J. Mater. Chem. A, 2026, 14, 7541–7551 | 7541

architectures such as films,[19] fibers,[7] and porous 3D-structures.[20]

This versatile dispersibility also allows MXenes to be integrated with various polymers,[21,22] metals[23] and ceramics,[24] expanding their applications into flexible coatings,[8,25] and composite materials.[26,27] Furthermore, the ability to disperse MXenes in a wide range of solvents, including ethanol, dimethyl formamide (DMF), dimethyl sulfoxide (DMSO),[15,22] enables precise control over their deposition and patterning,[28] supporting the development of advanced devices with tailored properties.[29,30] These collective advances in MXene processing represent a significant step toward realizing their full practical potential.

While organic solvents expand the application domain of MXenes, residual traces often remain after processing. These residues create localized areas of high resistance and increased interlayer spacing, which collectively lower overall conductivity.[21,22,31] For example, intercalated organic compounds such as tetramethyl ammonium hydroxide (TMAOH) have been found to increase the resistance of MXene-based devices, with resistance decreasing by only 20% after vacuum storage and 18% after annealing at 200 °C.[32] However, the factors affecting electrical conductivity loss during redispersion in organic solvents are not fully understood. One overlooked factor is the sheet damage during repeated solvent–exchange cycles. Prolonged mechanical agitation during synthesis has been previously reported to introduce defects and reduce sheet size,[33] and this type of physical damage may also happen during MXene processing and contribute to conductivity loss.

Earlier studies also overlooked conductivity loss in solvent-processed MXenes primarily due to inconsistent solvent exchange procedures, often using sonication for redispersion, which made the cause of structural or functional damage difficult to identify.[15,22] As a result, solvent-related conductivity variations were commonly attributed to secondary artefacts such as restacking or residual solvent rather than intrinsic interlayer phenomena. This highlighted the need for systematic investigation, particularly for MXene architectures involving extensive solvent processing such as fibers, aerogels, and composites. Recent work has demonstrated that phase changes in nanoconfined water between MXene layers drive changes in sheet orientation, interlayer spacing and electronic transport, establishing a link between MXene interfacial chemistry and conductivity.[34] Expanding on this understanding, we further examine how solvent exchange influences physical attributes, including the emergence of structural defects and morphological changes that can persist after solvent removal, leading to irreversible conductivity decrease despite nominally reversible interlayer spacing recovery.

In this study, we found that the electrical conductivity of $Ti_3C_2T_x$ MXene decreases after repeated washing in Milli-Q water. Conductivity dropped from ~2110 S cm^{-1} to ~1870 S cm^{-1} after one and three washing cycles, respectively, and further declined to ~1240 S cm^{-1} after five cycles due to cumulative sheet damage and oxidation. This sheet damage exacerbates the conductivity reduction caused by intercalated solvents during organic solvent processing. Dispersion in

DMSO and ethanol exhibited conductivities of only ~500 S cm^{-1} and ~888 S cm^{-1}, respectively. Even when organic-solvent-dispersed MXenes were exchanged back to water, restoring their original interlayer spacing (d-spacing ~1.34–1.38 nm), their conductivity remained lower than that of pristine $Ti_3C_2T_x$ MXene. Notably, neither the use of volatile solvents nor annealing at temperatures up to 200 °C restored conductivities to pristine levels. Instead, the final conductivity matched that of the water-washed samples subjected to the same number of redispersion cycles (<1200 S cm^{-1}), implying that sheet degradation is irreversible. These findings demonstrate that the conductivity loss stems not only from solvent intercalation but also from permanent structural damage incurred during processing.

Results and discussion

Structural degradation during repeated centrifuge-shaking cycles

Repeated washing was performed in Milli-Q water using a modified centrifugation-redispersion method adapted from our previous work.[22] Briefly, the initial aqueous $Ti_3C_2T_x$ MXene dispersion (~30 mg mL^{-1}) was centrifuged at 24 630 g for 45 minutes. The resulting pellet was then resuspended in fresh Milli-Q water using a vortex mixer for 10 min. This washing cycle was repeated 1×, 3×, or 5× times to achieve desired washing cycles and processing time (Fig. 1a).

Dynamic light scattering (DLS) analysis indicated that the average sheet size remained largely unchanged even after five washing cycles (Fig. 1b). Consistent with this, both (scanning electron microscope) SEM and (atomic force microscope) AFM images showed that the overall sheet dimensions were preserved. Although particle size remained largely unchanged after five water redispersions, the zeta potential increased from approximately −36 mV to −28 mV (Fig. 1c), suggesting surface alterations likely caused by exposed defects and oxidized areas, as also observed in the SEM and AFM images (Fig. 1d, e and S3).

These findings suggest that, unlike the degradation observed during MXene synthesis, mechanical stress from vortex mixing in this washing process was insufficient to break sheets into smaller fragments but still caused localized damage. One control pristine sample (Fig. S2) was left to stand for 4 h, matching the duration of the fully washed samples (5×). Its AFM and SEM features were comparable to those of the 1× sample, which was immediately prepared for AFM and SEM analysis and stored under vacuum to prevent water-induced degradation. The minimal cracks and defects in the unshaken sample suggest that the damage observed in the shaken samples resulted from vortex shaking.

Another control set of dispersions prepared using 20 minutes of manual shaking instead of vortex mixing exhibited similar, though less pronounced, structural degradation (Fig. S4). This indicates that prolonged mechanical agitation, even at lower intensities, can still compromise sheet integrity.

We propose that the pinholes observed in SEM images are primarily induced by turbulent forces exerted on the sheets from collisions with solvent molecules and neighbouring
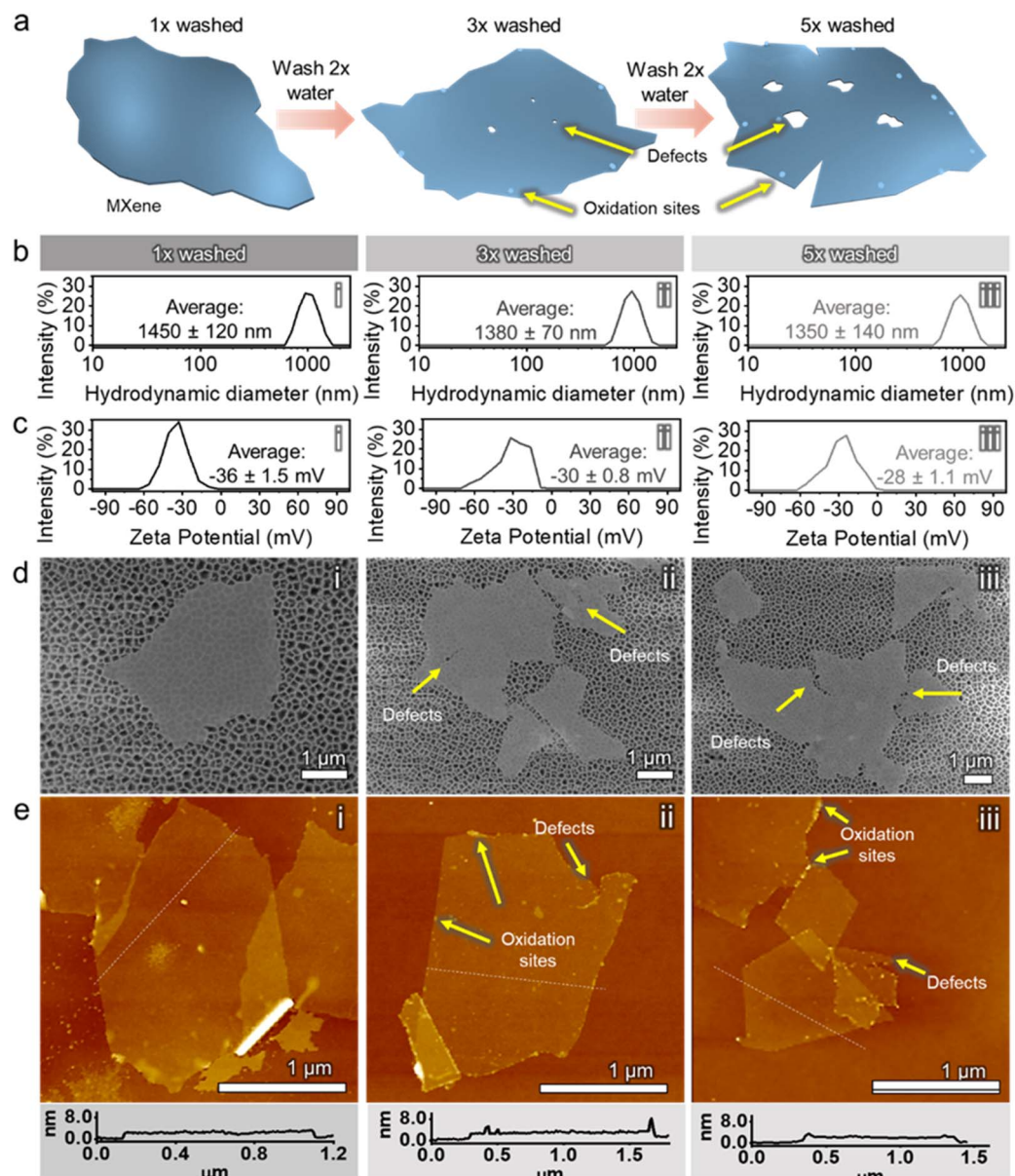
7542 | J. Mater. Chem. A, 2026, 14, 7541–7551

This journal is © The Royal Society of Chemistry 2026

Fig. 1 (a) Schematic illustration of the formation of defects and oxidation sites in $Ti_3C_2T_x$ MXene sheets after successive washing cycles. (b) Dynamic light scattering (DLS) size distribution and (c) zeta potential profiles, (d) scanning electron microscopy (SEM) images, and (e) atomic force microscopy (AFM) profiles of the $Ti_3C_2T_x$ MXene sheets after 1, 3, and 5 washing cycles.

MXene particles during mechanical agitation in solvent exchange. While the precise mechanism governing the formation of in-plane holes remains unclear, water-induced hydrolysis likely contributes to this process. Literature reports indicate that hydrolysis predominantly leads to oxide formation at sheet edges, where Ti-atoms are more exposed.[35,36] However, pre-existing in-plane defects in the initial MXene sheets may also act as starting sites for such degradation as they similarly have exposed Ti atoms like the edges of the sheets.

Although not clearly visible in SEM images, AFM analysis of individual $Ti_3C_2T_x$ MXene sheets (Fig. 1e) and X-ray photoelectron spectroscopy (XPS) analysis of films constructed from the dispersions (images on Fig. 2a–c and spectra on Fig. 2d–f) collectively reveal that increasing washing cycles lead to progressively higher oxide content, a known factor in reducing electrical conductivity.[37–39] The appearance and growth of grainy features at the sheet edges, as revealed by the AFM line-profile analysis in Fig. 1e, serve as strong indications of oxidation, with the 1×, 3×, and 5× washed samples exhibiting a progressive increase in the prominence of these features. Furthermore, roughness values derived from the same AFM datasets (Fig. S3) show that the root mean square roughness (R_q) increases from approximately 0.83 nm for the pristine sample to around 1.05 nm for the MXene washed five times, providing additional visual evidence of surface oxidation.
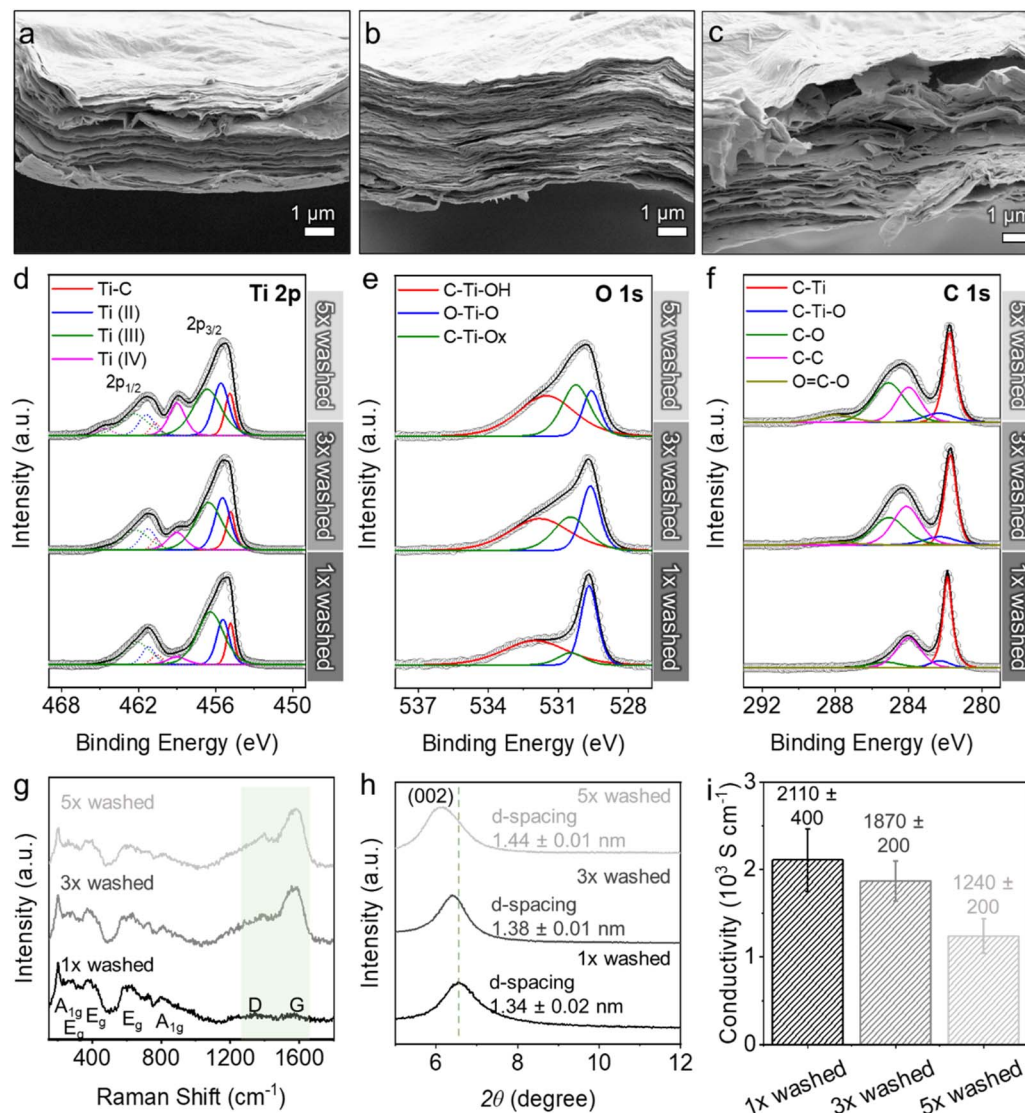
This journal is © The Royal Society of Chemistry 2026

J. Mater. Chem. A, 2026, 14, 7541–7551 | 7543

Fig. 2 (a–c) Cross-sectional SEM images of films prepared from 10 mL of 1 mg mL^{-1} dispersions of Ti$_3$C$_2$T$_x$ MXene sheets washed 1×, 3×, and 5× times in water. (d–f) High-resolution XPS spectra of the films shown in (a–c): stacked (d) Ti 2p, (e) O 1s, and (f) C 1s core-level spectra. (g) Raman spectra, (h) XRD patterns, and (i) electrical conductivity values of the same film samples.
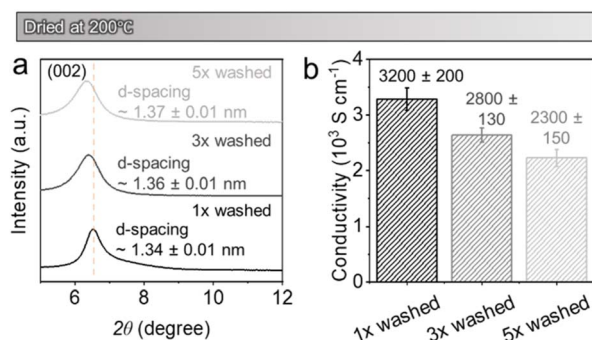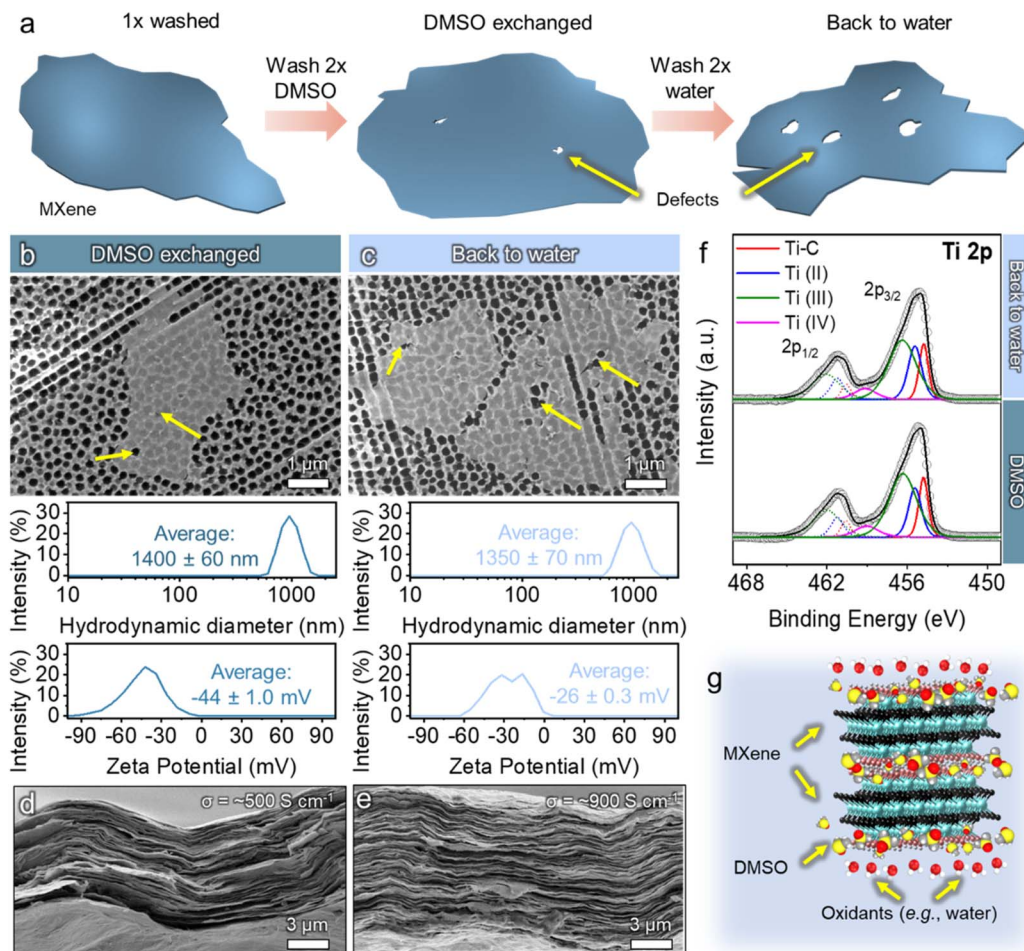

Fig. 3 (a) XRD patterns and (b) electrical conductivity values of film samples prepared from MXene washed in water with 1×, 3× and 5× cycles after vacuum annealing at 200 °C.

Moreover, the area of the Ti(IV) 2p$_{3/2}$ and 2p$_{1/2}$ peaks (at ∼459 eV and ∼464 eV) in the Ti 2p core spectra show a marked upward trend with washing. For instance, in pristine (1× washed) samples, these peaks account for ∼4.98% and ∼0.73%, rising to ∼8.17% and ∼0.90% after 3 washes, and further to ∼14.54% and ∼3.11% after 5 washes, confirming progressive surface oxidation (Fig. 2d and Tables S1–S3). Overall, this represents a three- to four-fold increase in oxidized Ti species after five washing cycles.

Similarly, the O 1s peaks corresponding to C–Ti–OH (∼531 eV) and C–Ti–O$_x$ (∼530 eV) increase steadily from ∼47.32% and ∼10.38% in pristine samples to ∼50.14% and ∼31.55% after five washing cycles, suggesting enhanced interaction with strongly hydrogen-bonding species, such as confined water (Fig. 2e and Tables S1–S3).[40] The O=C–O peak in the C 1s spectra (at ∼288 eV) also increased sharply from ∼0.49% to

7544 | J. Mater. Chem. A, 2026, 14, 7541–7551

This journal is © The Royal Society of Chemistry 2026

Fig. 4 (a) Schematic illustration of the solvent exchange process from water to DMSO and subsequent redispersion back into water. SEM images and corresponding DLS size distribution and zeta potential profiles of sheets after (b) exchange to DMSO and (c) re-dispersion in water. (d and e) Cross-sectional SEM images and (f) stacked Ti 2p core XPS spectra of films fabricated from the dispersions shown in (b) and (c). (g) Diagram illustrating the proposed protective mechanism of MXene against oxidation by water molecules.

~6.60%, indicating progressive oxidation of carbon components, particularly at defect sites (Fig. 2f and Tables S1–S3).

These results were supported by Raman spectroscopy, which showed increased D and G band intensities (~1360 cm^{-1} and ~1580 cm^{-1}) after 3× and 5× washes, further confirming progressive oxidation (Fig. 2g). This oxidation led to greater interlayer spacing, as shown by a shift in the (002) X-ray diffraction (XRD) peak from ~1.34 nm (1× wash) to ~1.44 nm (5× wash), likely due to trapped water and edge oxide formation (Fig. 2h). Collectively, these factors reduced the electrical conductivity of the films from approximately ~2110 S cm^{-1} (1× wash) to ~1870 S cm^{-1} (3× wash), and further to ~1240 S cm^{-1} after 5 wash cycles (Fig. 2i).

Even after vacuum annealing at 200 °C to remove most adsorbed water, samples washed 3× and 5× exhibited higher d-spacing (~1.36 nm and ~1.37 nm, respectively) than the annealed pristine samples (~1.34 nm) (Fig. 3a). Although annealing restored electrical conductivity in all sample, the final values for the 3× and 5× washed samples (~2800 S cm^{-1} and ~2300 S cm^{-1}, respectively) remained lower than that of the pristine sample (~3200 S cm^{-1}) (Fig. 3b). We attribute this overall increase in d-spacing and the reduction in conductivity to incomplete solvent removal and irreversible oxide formation at the sheet edges, as evidenced by AFM images. Moreover, the asymmetric XRD peak profiles likely reflect heterogeneities within the sheets, such as fully dried regions, areas containing residual solvent, and regions with embedded oxide grains.

Loss of conductivity when using organic solvent (DMSO)

To mitigate water-induced degradation, Ti$_3$C$_2$T$_x$ MXene was processed in DMSO using the same centrifugation–redispersion procedure, leveraging DMSO's known protective properties (Fig. 4a).[15,22,41] Samples in DMSO yielded a zeta potential of approximately −44 mV, indicating a more stable dispersion than those in water (Fig. 4c).

While this approach successfully limited chemical oxidation, it introduced structural defects. SEM imaging revealed that DMSO processing caused cracks and holes in the MXene sheets (Fig. 4b). However, a corresponding DLS profile showed a consistent sheet size distribution (Fig. 4b), indicating that the
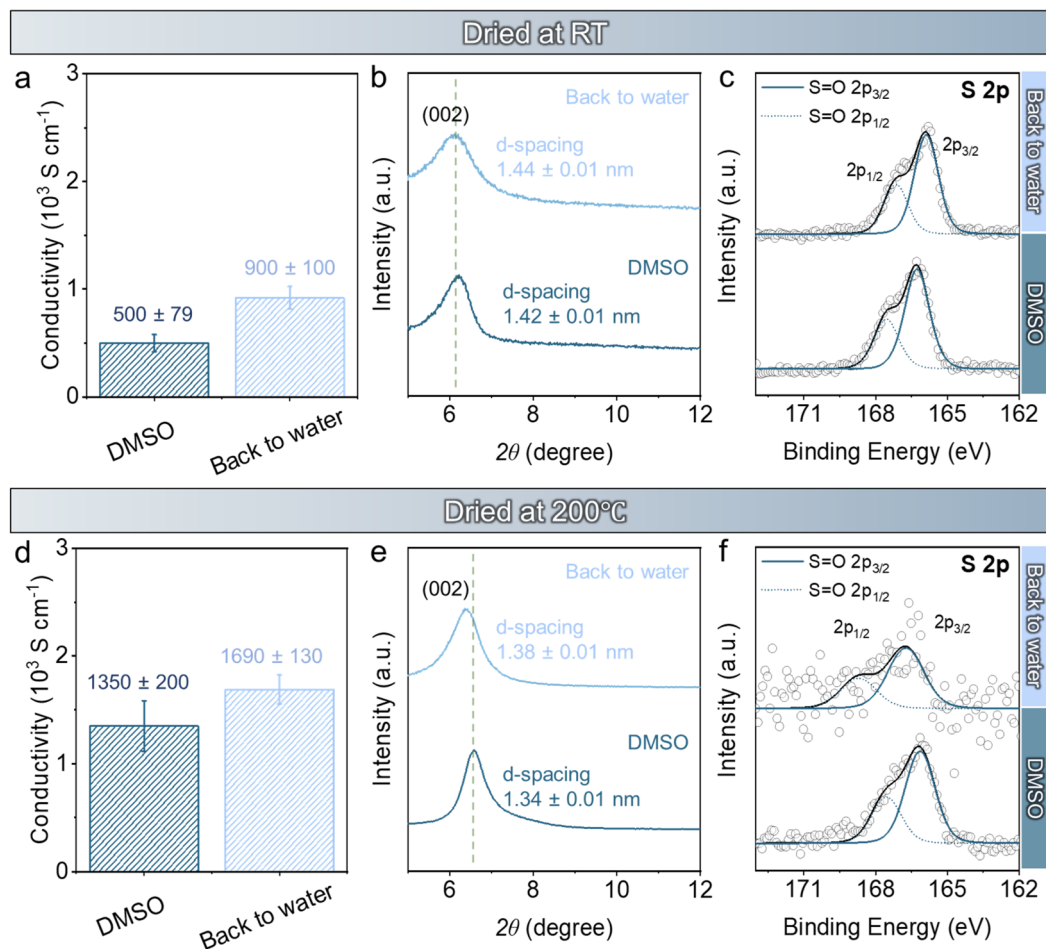
Fig. 5 Comparison of (a) electrical conductivity, (b) XRD patterns, and (c) S 2p XPS spectra of $Ti_3C_2T_x$ MXene films dried at room temperature and (d–f) after annealing at 200 °C for 12 hours. Films were prepared from MXene stored in DMSO (dark blue) and MXene redispersed in water after DMSO exchange (light blue).

damage was limited to surface features rather than a complete fragmentation into smaller sheets.

The protective effect of DMSO was clearly demonstrated by XPS data. The Ti 2p spectra of DMSO-processed films showed only minimal Ti(IV) peaks at ~459 eV ($2p_{3/2}$) and ~464 eV ($2p_{1/2}$), with abundances of ~5.90% and ~0.63%, respectively (Fig. 4f and Table S4). These values are notably low and comparable to those of pristine samples (washed only 1× with water; Fig. 2d and Table S1), and significantly lower than samples subjected to multiple water-washing cycles (3×, 5×; Fig. 2d and Tables S2–S3).
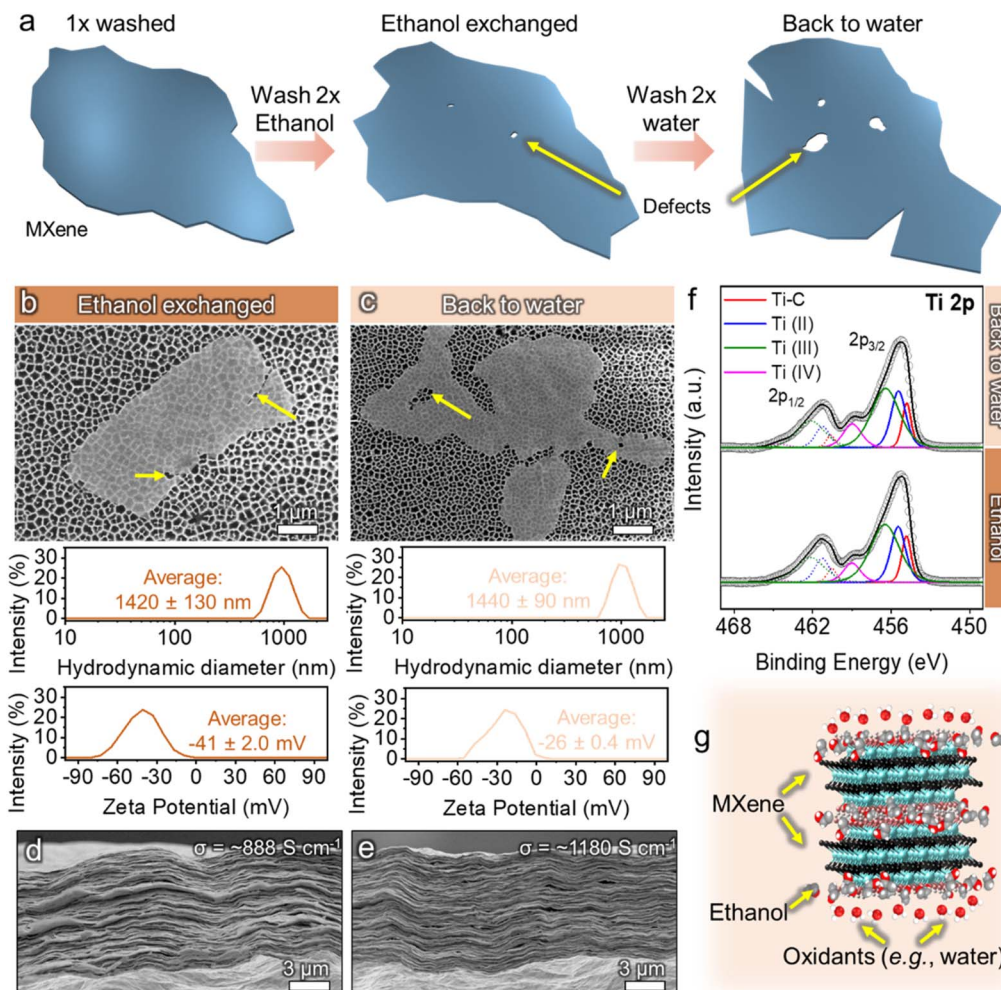
To evaluate the persistence of this protection, the DMSO dispersion was redispersed back into water. This process also led to further crack formation, which exposed additional defects and caused the zeta potential to shift to approximately −26 mV (Fig. 4c). Nevertheless, these structural damages had a negligible impact on the overall sheet size. Crucially, the low Ti(IV) content was preserved, with peak abundances remaining at ~5.74% and ~0.57% (Fig. 4f). This result confirms that DMSO provides a durable protective effect against oxidation even after the solvent removal, highlighting its efficacy in stabilizing $Ti_3C_2T_x$ MXene (Fig. 4g).

To further investigate the role of trapped solvent molecules, we characterized the electrical conductivity, XRD, and XPS of MXene films (Fig. 4d and e) under two conditions: dried at room temperature (RT) and annealed at 200 °C. This annealing temperature was selected to remove a significant portion of the solvent. However, it is important to note that complete removal of all nano-confined solvents from $Ti_3C_2T_x$ MXene is challenging, even at temperatures up to 600 °C.[42]

As anticipated, RT-dried films from DMSO-dispersed MXene exhibited low electrical conductivity of ~500 S cm^{-1} (Fig. 5a). Films made from DMSO-processed MXene that was redispersed back into water showed only a modest improvement to ~900 S cm^{-1}, a value still lower than that of samples washed solely with water (~1200 S cm^{-1}). This reduced conductivity correlates with an enlarged interlayer spacing of ~1.42 nm and ~1.44 nm for the DMSO and water-redispersed samples, respectively (Fig. 5b), which impedes electron transport between sheets. The presence of residual DMSO was confirmed by XPS, which detected sulfur (S) atomic contents of ~3.18% and ~3.10% in the respective samples (Fig. 5c and Table S8). This residual solvent likely contributes to the expanded

7546 | *J. Mater. Chem. A*, 2026, **14**, 7541–7551

This journal is © The Royal Society of Chemistry 2026

Fig. 6 Impact of ethanol solvent exchange on $Ti_3C_2T_x$ MXene. (a) Schematic of the solvent exchange process to ethanol and subsequent re-dispersion in water. This process can promote defect and oxidation site formation. (b and c) SEM images and corresponding DLS size distribution and zeta potential profiles of sheets after (b) ethanol exchange and (c) water redispersion. (d and e) Cross-sectional SEM images and (f) stacked Ti 2p XPS spectra of films fabricated from the dispersions shown in (b) and (c). Proposed protective mechanism of ethanol against oxidation.

interlayer spacing and the persistently low Ti(IV) content, as previously observed in Fig. 4f.

Annealing at 200 °C for 12 hours led to a huge recovery of electrical conductivity, with values increasing to ~1350 S cm^{-1} and ~1690 S cm^{-1}, for the DMSO-dispersed and water-redispersed samples, respectively (Fig. 5d). This improvement coincided with a reduction in interlayer spacing to ~1.34 nm and ~1.38 nm (Fig. 5e), indicating the partial removal of trapped solvent molecules. Correspondingly, the sulfur content detected by XPS dropped sharply to $\sim1.33\%$ and $\sim0.09\%$ atomic content (Fig. 5f and Table S8).

However, the persistence of a detectable S signal even after annealing suggests that DMSO is strongly bound to the MXene layers. This is likely due to strong ionic interactions between the charged resonance structure of DMSO $(CH_3S^+O^-CH_3)$[43] and the $Ti_3C_2T_x$ MXene surface, making it difficult to remove completely. Nevertheless, the presence of intercalated species such as DMSO, which increase the interlayer spacing, may not be entirely detrimental to MXenes. Though it reduces electrical conductivity, it can enhance interlayer transport by expanding the spacing and facilitating ion diffusion through the nanoscale channels, and has been shown to benefit electrochemical applications.[44,45]

Using a volatile organic solvent (ethanol)

To eliminate persistent solvent effects, ethanol was tested as an alternative protective agent due to its volatile nature, which should allow for easier removal than DMSO (Fig. 6a). MXene was redispersed in ethanol, forming a stable dispersion with zeta potential of approximately -41 mV. Similarly, a comparable set of samples was subsequently redispersed back into water to evaluate the efficacy of solvent removal through washing (Fig. 6a).

Similar to DMSO, exchange with ethanol caused mechanical degradation, with SEM images revealing holes and cracks (Fig. 6b and c). DLS profiles remained consistent (Fig. 6b), confirming that the sheets were not fragmented. Redispersion back into water had a negligible effect on sheet size but exacerbated the formation of holes and cracks, resulting in a zeta potential of approximately-26 mV (Fig. 6c).
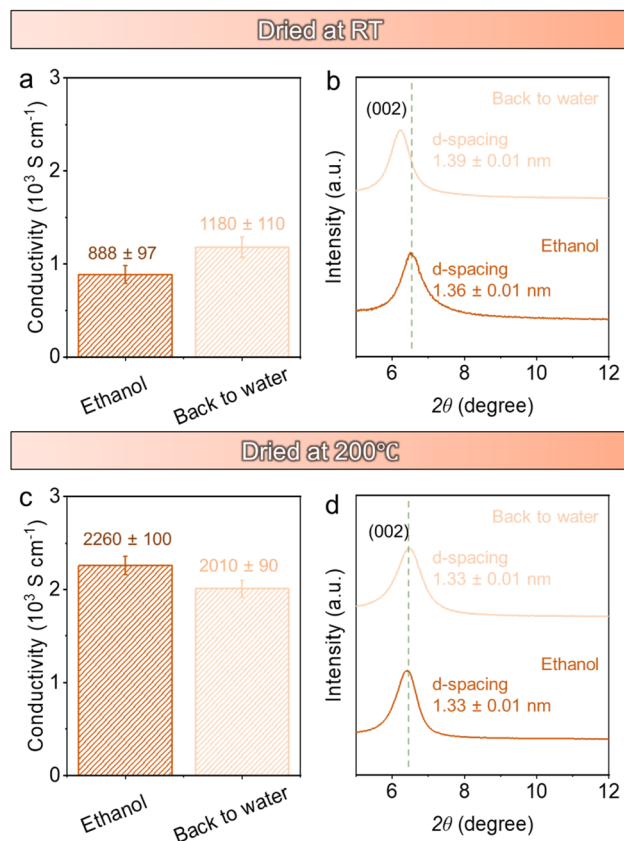
Fig. 7 Effect of annealing on ethanol-processed MXene films. (a and c) Electrical conductivity and (b and d) XRD patterns for films dried at room temperature. Data is shown for films prepared from MXene dispersion in ethanol and MXene redispersed in water after ethanol and MXene redispersed in water after ethanol exchange.

XPS analysis revealed that films prepared from ethanol-dispersed MXene exhibited Ti(IV) $2p_{3/2}$ and $2p_{1/2}$ peaks abundances of ~7.71% and ~0.85%, respectively (Fig. 6f and Table S9). These values indicate a moderate level of oxidation, higher than in DMSO-processed samples but lower than water-processed ones, highlighting the partial protective effect this organic solvent (Fig. 6g). Ethanol enhances MXene's oxidation resistance through surface protection, similar to DMSO (Fig. 6g). The presence of ethanol on the MXene surface likely mitigates water exposure, as ethanol can form an azeotropic mixture with water, thereby favouring ethanol–water interactions over direct MXene-water contact.[46] However, when the ethanol-processed MXene was redispersed back into water, the Ti(IV) peaks increased significantly to ~9.70% and ~1.63% (Fig. 6f and Table S10). This greater susceptibility to oxidation upon water reintroduction, compared to the durable protection offered by DMSO, demonstrates that ethanol is a less effective barrier against oxidants.

To assess the effect of residual solvent, films from ethanol-processed MXene were prepared by drying at RT and annealing at 200 °C. Despite ethanol's volatility, the RT-dried films exhibited significantly reduced electrical conductivity. Films from ethanol-dispersed MXene measured ~888 S cm^{-1} (Fig. 7a) while those redispersed back into water only reached ~1180 S cm^{-1}. These values are remarkably lower than those of pristine (~2110 S cm^{-1}, Fig. 2i) and 3× water-washed MXene (~1870 S cm^{-1}). This decreased performance is attributed to an enlarged interlayer spacing of ~1.36 and ~1.39 nm, for the respective samples (Fig. 7b), compared to ~1.34 nm for pristine MXene (Fig. 2h). The expanded spacings represent trapped solvent molecules between the MXene layers, which increases contact resistance and degrades conductivity.

Annealing at 200 °C for 12 hours successfully restored the electrical conductivity of the ethanol-processed MXene films, with values reaching ~2260 S cm^{-1} and ~2010 S cm^{-1} for the ethanol-dispersed and water-redispersed samples, respectively (Fig. 7c). This recovery coincided with a reduction in interlayer spacing to approximately ~1.33 nm for both samples (Fig. 7d), a value comparable to that of unannealed pristine MXene. This suggests that annealing effectively removed most of the intercalated solvent molecules, allowing the layers to pack more tightly and reducing inter-sheet contact resistance.

Unlike DMSO, ethanol does not contain any sulfur or other unique elemental markers, making residual solvent difficult to detect via XPS. The observed contraction in interlayer spacing therefore serves as the primary evidence for solvent removal. However, despite achieving a similar interlayer spacing to annealed pristine MXene (~1.34 nm, Fig. 2h), the conductivity of the ethanol-processed samples remained significantly lower (~2260/2010 vs. ~3250 S cm^{-1}). This discrepancy implies that while annealing removes most trapped solvents, the additional solvent exchange cycles themselves cause irreversible damage, such as holes and cracks (as seen in SEM images). Importantly, even at 600 °C, some nano-confined molecules (both water and ethanol) may persist on the surface and lattice of MXene.[42] Annealing at 200 °C primarily eliminates the volatile solvents trapped between layers, restoring the interlayer spacing to a baseline condition that still includes surface-bound water molecules.

Conclusions

The electrical conductivity of solvent-processed Ti$_3$C$_2$T$_x$ MXenes is fundamentally limited by irreversible processes arising from the combined effects of structural damage, oxidation, and residual solvents. Vigorous agitation during redispersion generates defects such as holes, cracks, and layer delamination, permanently disrupting the conductive network within individual MXene sheets. At the same time, residual solvents can intercalate between MXene layers, expanding the interlayer spacing and creating high-resistance regions, while oxidation of exposed surfaces further degrades electronic pathways. Residual solvents may additionally intercalate between MXene layers, increasing interlayer spacing and creating high-resistance regions. However, even after solvent removal via annealing or volatile solvent exchange, the electrical conductivity does not recover to pristine levels. This incomplete recovery of electrical conductivity reflects the irreversible nature of structural damage and oxidation rather than reversible solvent effects alone. Notably, trace amounts of water have been reported to persist within MXene interlayers up to ~600 °C, facilitating continued oxidation of defect-rich regions. Collectively, these results demonstrate that mechanical sheet degradation leads to irreversible conductivity loss, primarily due to oxidation-driven

disruption of the conductive network. This understanding highlights the need for processing strategies that minimize mechanical agitation and oxidative exposure to preserve the intrinsic electrical performance of MXenes for advanced applications.

Experimental

Synthesis of MXene

The minimally intensive layer delamination (MILD) method was employed to synthesize single-to-few layer $Ti_3C_2T_x$ MXene sheets.[22,35,44,47–49] Specifically, the aluminum layer was selectively etched from a Ti_3AlC_2 MAX phase precursor (1 g, < 40 μm, Carbon-Ukraine Ltd) using hydrofluoric acid generated *in situ* from a mixture of 1.6 g lithium fluoride (LiF, 99%, Sigma-Aldrich) in 20 mL 9 M hydrochloric acid (HCl, 12 M, Sigma-Aldrich).

The etching solution was pre-stirred for 5 minutes before the Ti_3AlC_2 MAX phase was carefully added. The resulting suspension was then vigorously stirred (500 rpm) at room temperature for 30 hours. This process yielded a mixture of multi-layer MXene and partially etched MAX phase. The mixture was centrifuged (Thermo Scientific Multifuge X3R) at 3500 rpm (1331 rcf) for 15 minutes. This centrifugation-redispersion cycle was repeated until the dispersion reached a near-neutral pH (∼6) and predominantly contained single-layer sheets.

To remove the remaining partially etched MAX phase, the dispersion underwent a low-speed centrifugation (1500 rpm, 244 rcf) for 15 minutes. The dark green supernatant, containing the desired single-layer MXene sheets, was recovered. This supernatant was then centrifuged at a high speed (7000 rpm, 5323 rcf) for 30 minutes to concentrate the MXene into a gel-like pellet.

The MXene concentration was determined by vacuum-drying a 25 μL aliquot of the sediment in a pre-weighed aluminum pan for 1 to 2 hours and measuring the mass. Finally, the sediment was reconcentrated to 5 mg mL^{-1} using Ar-purged Milli-Q water and stored at −20 °C until further use.

Solvent transfer into organic solvents

The solvent transfer method was adapted from previous literature.[22] Briefly, the parent aqueous MXene dispersion was repeatedly centrifuged at 15 000 rpm (24 630 g) for 1 hour. After each centrifugation step, the supernatant was carefully discarded and replaced with the chosen solvent (anhydrous DMSO or 200-proof ethanol). After each centrifugation step, the supernatant was carefully discarded and replaced with the chosen solvent (anhydrous DMSO or 200-proof ethanol). The mixture was then redispersed by vortex mixing (Ratek VM1) for 10 minutes at 2700 rpm. This cycle was repeated at least twice to ensure the extensive removal of water.

Redispersion to water

Solvent exchanged MXenes were subjected to a reverse transfer process back into Milli-Q water to eliminate residual organic solvent. Briefly, the dispersion was centrifuged (15 000 rpm, 24 630 g, ThermoScientific Heraeus Multifuge X3R) for 1 h. The supernatant was then carefully discarded and replaced with Milli-Q water, followed by redispersion of the pellet by vigorous vortex

mixing (Ratek) for 10 minutes. A minimum of two washing cycles was performed to minimize the organic solvent content.

Preparation of film samples

The dispersions were vacuum-filtered to form films using a glass microfiltration apparatus fitted with a fritted sand-supported base and a 45 mm diameter polypropylene membrane (Celgard 3501, pore size 0.22 μm). The films were stored in a vacuum desiccator pending further characterization.

Characterization

A comprehensive suite of techniques was employed to characterize MXene samples. The size distribution of $Ti_3C_2T_x$ dispersions was determined by dynamic light scattering (DLS) using a Nano ZS Zetasizer (Malvern Instruments, UK). For each measurement, 1 mL of a 10 μg mL^{-1} dispersion was placed in a quartz cuvette, with data representing the average of five replicates and five repeat measurements per replicate.

Films for structural and electrical analysis were prepared by vacuum filtration. For cross-sectional scanning electron microscopy (SEM) imaging, films were mounted vertically on custom-made aluminium stubs. All other films were mounted on a zero-background SiO_2 substrate for X-ray diffraction (XRD) analysis, which was performed using a PANalytical X'Pert Powder diffractometer with Cu Kα radiation (λ = 1.54 Å), a 2θ scan step of 0.013°, and 100 ms dwell time.

SEM imaging was conducted on a Supra 55-VP field emission scanning electron microscope (Zeiss, Germany) at an accelerating voltage of 3 keV using. Samples from dispersions were prepared by drop-casting a 50-μg mL^{-1} dispersion onto anodic discs and vacuum-drying for 24 hours.

Raman spectra were acquired using a Renishaw InVia Raman Microspectrometer (UK) with a 514 nm Ar ion laser at 5% laser power, a 2400 I mm^{-1} grating, a 20 s acquisition time, and 3 accumulations.

X-ray photoelectron spectroscopy (XPS) was performed using a K-Alpha + system (Thermo Fisher Scientific, USA). Film samples were secured to the holder with conductive carbon tape. Survey scans (0 to 1350 eV, 200 eV pass energy, 1 eV resolution) and high-resolution core spectrum (50 eV pass energy, 0.1 eV step) for titanium, carbon, oxygen, and sulfur were acquired under an ultra-high vacuum (5×10^{-8} mbar). Three locations per sample were analyzed with 10 scans per location. Data processing, including background correction, normalization, deconvolution, and peak fitting, were conducted using CasaXPS software. Atomic percentages for sulfur in DMSO-redispersed samples were quantified using C, Ti, O, F and N peaks from the survey spectra.

The electrical conductivity (σ) of the films was measured using an Ossila Four-Point Probe System (UK) with a probe spacing of 1.27 mm. Five samples with lateral dimensions of 1 cm × 1 cm were measured, with five measurements taken per sample. Film thicknesses used for conductivity normalization were obtained from cross-sectional SEM images and quantified in ImageJ (Fig. S5). Conductivity values were calculated and reported by the Ossila Sheet Resistance® software.

This journal is © The Royal Society of Chemistry 2026

J. Mater. Chem. A, 2026, **14**, 7541–7551 | **7549**

Error bars were included for key quantitative data acquired above to represent experimental variability. We note that these variations arise from inherent experimental uncertainty and do not affect the overall conclusions. For completeness, standard errors are also reported for unplotted data (*e.g.*, XRD, DLS, and zeta potential insets) where error bars could not be displayed graphically.

Author contributions

Ken Aldren S. Usman: conceptualization, investigation, validation, visualization, writing – original draft, Joselito M. Razal: conceptualization, validation, writing – review & editing, Babak Anasori: validation, writing – review & editing, Rochelle P. Ibabao: investigation, writing – review & editing, Kim Marie D. Sisican: investigation, writing – review & editing, Mia Judicpa: investigation, writing – review & editing, Rufus Mart Ceasar R. Ramos: writing – review & editing, Kevinilo P. Marquez: investigation, writing – review & editing, Elmer S. Austria Jr.: investigation, writing – review & editing, Behnam Akhavan: investigation, writing – review & editing, Anupma Thakur: investigation, validation, writing – review & editing, Nithin Chandran B. S.: investigation, validation, writing – review & editing, Jizhen Zhang: validation, writing – review & editing, Luke C. Henderson: validation, writing – review & editing.

Conflicts of interest

There are no conflicts to declare.

Data availability

All data are available in the supplementary information (SI) and upon request to the authors. Supplementary information is available. See DOI: https://doi.org/10.1039/d5ta09004k.

Acknowledgements

References

1 M. Naguib, M. Kurtoglu, V. Presser, J. Lu, J. Niu, M. Heon, L. Hultman, Y. Gogotsi and W. Barsoum Michel, *Adv. Mater.*, 2011, **23**, 4248–4253.

2 M. Naguib, J. Come, B. Dyatkin, V. Presser, P.-L. Taberna, P. Simon, M. W. Barsoum and Y. Gogotsi, *Electrochem. Commun.*, 2012, **16**, 61–64.

3 G. Deysher, C. E. Shuck, K. Hantanasirisakul, N. C. Frey, A. C. Foucher, K. Maleski, A. Sarycheva, V. B. Shenoy, E. A. Stach, B. Anasori and Y. Gogotsi, *ACS Nano*, 2020, **14**, 204–217.

4 A. Shayesteh Zeraati, S. A. Mirkhani, P. Sun, M. Naguib, P. V. Braun and U. Sundararaj, *Nanoscale*, 2021, **13**, 3572–3580.

5 T. S. Mathis, K. Maleski, A. Goad, A. Sarycheva, M. Anayee, A. C. Foucher, K. Hantanasirisakul, C. E. Shuck, E. A. Stach and Y. Gogotsi, *ACS Nano*, 2021, **15**, 6420–6429.

6 C. Yang, Y. Tang, Y. Tian, Y. Luo, M. Faraz Ud Din, X. Yin and W. Que, *Adv. Energy Mater.*, 2018, **8**, 1802087.

7 J. Zhang, S. Uzun, S. Seyedin, P. A. Lynch, B. Akuzum, Z. Wang, S. Qin, M. Alhabeb, C. E. Shuck, W. Lei, E. C. Kumbur, W. Yang, X. Wang, G. Dion, J. M. Razal and Y. Gogotsi, *ACS Cent. Sci.*, 2020, **6**, 254–265.

8 S. Qin, K. A. S. Usman, D. Hegh, S. Seyedin, Y. Gogotsi, J. Zhang and J. M. Razal, *ACS Appl. Mater. Interfaces*, 2021, **13**, 36655–36669.

9 X. Li, Z. Huang, C. E. Shuck, G. Liang, Y. Gogotsi and C. Zhi, *Nat. Rev. Chem.*, 2022, **6**, 389–404.

10 F. Shahzad, M. Alhabeb, C. B. Hatter, B. Anasori, S. Man Hong, C. M. Koo and Y. Gogotsi, *Science*, 2016, **353**, 1137–1140.

11 H. Lin, X. Wang, L. Yu, Y. Chen and J. Shi, *Nano Lett.*, 2017, **17**, 384–391.

12 J. T. Lee, B. C. Wyatt, G. A. Davis, Jr., A. N. Masterson, A. L. Pagan, A. Shah, B. Anasori and R. Sardar, *ACS Nano*, 2021, **15**, 19600–19612.

13 X. Han, J. Huang, H. Lin, Z. Wang, P. Li and Y. Chen, *Adv. Healthc. Mater.*, 2018, **7**, 1701394.

14 R. B. Rakhi, P. Nayak, C. Xia and H. N. Alshareef, *Sci. Rep.*, 2016, **6**, 36422.

15 K. Maleski, V. N. Mochalin and Y. Gogotsi, *Chem. Mater.*, 2017, **29**, 1632–1640.

16 M. A. Hope, A. C. Forse, K. J. Griffith, M. R. Lukatskaya, M. Ghidiu, Y. Gogotsi and C. P. Grey, *Phys. Chem. Chem. Phys.*, 2016, **18**, 5099–5102.

17 D. Magne, V. Mauchamp, S. Célérier, P. Chartier and T. Cabioc'h, *Phys. Rev. B*, 2015, **91**, 201409.

18 B. Akuzum, K. Maleski, B. Anasori, P. Lelyukh, N. J. Alvarez, E. C. Kumbur and Y. Gogotsi, *ACS Nano*, 2018, **12**, 2685–2694.

19 Z. Ling, C. E. Ren, M.-Q. Zhao, J. Yang, J. M. Giammarco, J. Qiu, M. W. Barsoum and Y. Gogotsi, *Proc. Natl. Acad. Sci. U. S. A.*, 2014, **111**, 16676.

20 R. Bian, G. He, W. Zhi, S. Xiang, T. Wang and D. Cai, *J. Mater. Chem. C*, 2019, **7**, 474–478.

21 S. Seyedin, S. Uzun, A. Levitt, B. Anasori, G. Dion, Y. Gogotsi and J. M. Razal, *Adv. Funct. Mater.*, 2020, **30**, 1910504.

22 S. Seyedin, J. Zhang, K. A. S. Usman, S. Qin, A. M. Glushenkov, E. R. S. Yanza, R. T. Jones and J. M. Razal, *Glob. Chall.*, 2019, **3**, 1900037.

23 J. Patenaude, B. C. Wyatt, S. K. Nemani and B. Anasori, *MRS Adv.*, 2024, **9**, 551–556.

24 B. C. Wyatt, S. K. Nemani and B. Anasori, *Nano Convergence*, 2021, **8**, 16.

25 A. Levitt, J. Zhang, G. Dion, Y. Gogotsi and J. M. Razal, *Adv. Funct. Mater.*, 2020, **30**, 2000739.

7550 | *J. Mater. Chem. A*, 2026, **14**, 7541–7551

This journal is © The Royal Society of Chemistry 2026

26 A. Levitt, D. Hegh, P. Phillips, S. Uzun, M. Anayee, J. M. Razal, Y. Gogotsi and G. Dion, *Mater. Today*, 2020, **34**, 17–29.

27 S. Uzun, S. Seyedin, A. L. Stoltzfus, A. S. Levitt, M. Alhabeb, M. Anayee, C. J. Strobel, J. M. Razal, G. Dion and Y. Gogotsi, *Adv. Funct. Mater.*, 2019, **29**, 1905015.

28 Y. Z. Zhang, Y. Wang, Q. Jiang, J. K. El-Demellawi, H. Kim and H. N. Alshareef, *Adv. Mater.*, 2020, **32**, 1908486.

29 K. A. S. Usman, S. Qin, L. C. Henderson, J. Zhang, D. Y. Hegh and J. M. Razal, *Mater. Horiz.*, 2021, **8**, 2886–2912.

30 N. Kong, J. Zhang, D. Hegh, K. A. S. Usman, S. Qin, P. A. Lynch, W. Yang and J. M. Razal, *Nanoscale*, 2022, **14**, 6299–6304.

31 S. Seyedin, E. R. S. Yanza and J. M. Razal, *J. Mater. Chem. A*, 2017, **5**, 24076–24082.

32 J. L. Hart, K. Hantanasirisakul, A. C. Lang, B. Anasori, D. Pinto, Y. Pivak, J. T. van Omme, S. J. May, Y. Gogotsi and M. L. Taheri, *Nat. Commun.*, 2019, **10**, 522.

33 M. Shekhirev, J. Busa, C. E. Shuck, A. Torres, S. Bagheri, A. Sinitskii and Y. Gogotsi, *ACS Nano*, 2022, **16**, 13695–13703.

34 T. Zhang, K. A. Mazzio, R. J. Wang, M. Lounasvuori, A. Al-Temimy, F. Amargianou, M.-A. Mawass, F. Kronast, D. M. Többens, K. Lips, T. Petit and Y. Gogotsi, *Nat. Commun.*, 2025, **16**, 7447.

35 J. Zhang, N. Kong, D. Hegh, K. A. S. Usman, G. Guan, S. Qin, I. Jurewicz, W. Yang and J. M. Razal, *ACS Appl. Mater. Interfaces*, 2020, **12**, 34032–34040.

36 S. Huang and V. N. Mochalin, *Inorg. Chem.*, 2019, **58**, 1958–1966.

37 P. Flouda, S. A. Shah, D. C. Lagoudas, M. J. Green and J. L. Lutkenhaus, *Matter*, 2019, **1**, 1532–1546.

38 T. Zhao, J. Zhang, Z. Du, Y. Liu, G. Zhou and J. Wang, *Electrochim. Acta*, 2017, **254**, 308–319.

39 S. Wan, X. Li, Y. Wang, Y. Chen, X. Xie, R. Yang, A. P. Tomsia, L. Jiang and Q. Cheng, *Proc. Natl. Acad. Sci. U. S. A.*, 2020, **117**, 27154–27161.

40 J. Yang, M. Li, S. Fang, Y. Wang, H. He, C. Wang, Z. Zhang, B. Yuan, L. Jiang, R. H. Baughman and Q. Cheng, *Science*, 2024, **383**, 771–777.

41 K. P. Marquez, K. M. D. Sisican, R. P. Ibabao, R. A. J. Malenab, M. A. N. Judicpa, L. Henderson, J. Zhang, K. A. S. Usman and J. M. Razal, *Small Sci.*, 2024, 2400150.

42 H. Fang, A. Thakur, A. Zahmatkeshsaredorahi, Z. Fang, V. Rad, A. A. Shamsabadi, C. Pereyra, M. Soroush, A. M. Rappe, X. G. Xu, B. Anasori and Z. Fakhraai, *Proc. Natl. Acad. Sci. U.S.A*, 2024, **121**, e2400084121.

43 E. D. Glendening and A. L. Shrout, *J. Phys. Chem. A*, 2005, **109**, 4966–4972.

44 F. Yang, D. Hegh, D. Song, J. Zhang, K. A. S. Usman, Z. Wang, P. Zhang, W. Ma, W. Yang, S. Qin and J. M. Razal, *J. Mater. Chem. A*, 2021, **9**, 6393–6401.

45 X. Yin, W. Zheng, H. Tang, L. Yang, P. Zhang and Z. Sun, *J. Mater. Chem. A*, 2024, **12**, 8952–8962.

46 V. Carravetta, A. H. d. A. Gomes, R. d. R. T. Marinho, G. Öhrwall, H. Ågren, O. Björneholm and A. N. de Brito, *Phys. Chem. Chem. Phys.*, 2022, **24**, 26037–26045.

47 K. A. S. Usman, J. Zhang, D. Y. Hegh, A. O. Rashed, D. Jiang, P. A. Lynch, P. Mota-Santiago, K. L. Jarvis, S. Qin, E. L. Prime, M. Naebe, L. C. Henderson and J. M. Razal, *Adv. Mater. Interfaces*, 2021, **8**, 2002043.

48 D. Jiang, J. Zhang, S. Qin, Z. Wang, K. A. S. Usman, D. Hegh, J. Liu, W. Lei and J. M. Razal, *ACS Nano*, 2021, **15**, 5000–5010.

49 J. Zhang, E. Kerr, K. A. S. Usman, E. H. Doeven, P. S. Francis, L. C. Henderson and J. M. Razal, *Chem. Commun.*, 2020, **56**, 10022–10025.

This journal is © The Royal Society of Chemistry 2026

J. Mater. Chem. A, 2026, **14**, 7541–7551 | 7551